Electronic Supplementary Information (ESI) for:

"Expanding the tunability and applicability of exchange-coupled/decoupled magnetic nanocomposites"

Cecilia Granados-Miralles,*[a] Adrián Quesada,[a] Matilde Saura-Múzquiz,‡[b] Henrik L. Andersen, §[b] José F. Fernández,[a] and Mogens Christensen[b]

[a] Electroceramics Department, Instituto de Cerámica y Vidrio, CSIC, Kelsen 5, ES 28049 Madrid, Spain
[b] Center for Materials Crystallography, Department of Chemistry and iNANO, Aarhus University, Langelandsgade 140, DK 8000 Aarhus, Denmark

‡ Current address: School of Chemistry, University of Sydney, F11, NSW 2006 Sydney, Australia
§ Current address: School of Chemistry, UNSW Australia, NSW 2052 Sydney, Australia

* corresponding autor: c.granados.miralles@icv.csic.es

Contents

1. Experimental methods

1.1. Heating profiles

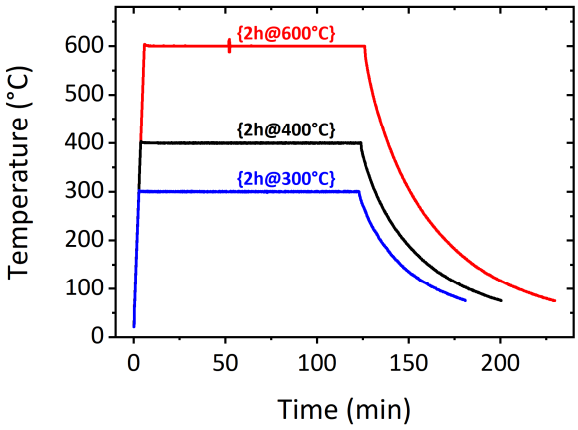

Figure S1. Heating profiles of the reduction treatments in the tubular furnace.

2. Structural characterization: powder X-ray diffraction

2.1. Note on measurement conditions

The PXRD measurements were performed in Bragg-Brentano configuration. In this measurement configuration, the obtained peak intensities are only trustworthy as long as the probed sample volume is the same for all 2θ values. The area illuminated at smaller angles is larger than at high angles, but at low angles, the penetration depth is shorter than at high angles. This results in the same volume probed for all 2θ angles (see Figure S2).

For very small 2θ angles it can happen that the illuminated area is greater than the sample area, *i.e.*, the sample is "overilluminated". When this happens the measurement is incorrect because the probed sample volume is smaller at low angles than it is for high angles. The threshold in 2θ below which the sample is overexposed is calculated in the Rigaku SmartLab user manual.

In the article, those samples for which the amount of powders was enough to fill the full sample holder were performed with an insident slit (IS) of 1/2° (see Figure S3). In this experimental configuration, the 2θ threshold is at 15° (green circle in Figure S3). Therefore, the diffractometer was set to collect data in the range 15-115°. The samples measured in this conditions were the starting material and the composites {2h@300°C}, {4h@300°C} and {2h@400°C}.

The most aggressive reduction treatments, {8h@300°C} and {2h@600°C}, resulted in an important mass loss and the obtained amount of sample was not enough to fill the whole sample holder. In this case, the sample width was approx. 5 cm (see Figure S4). To carry out these measurements, the incident slit was reduced to 1/6°. In these conditions, the calculated 2θ threshold is at 20° (red circle in Figure S4). Therefore, the diffractometer was set to collect data in the range 20-115°.

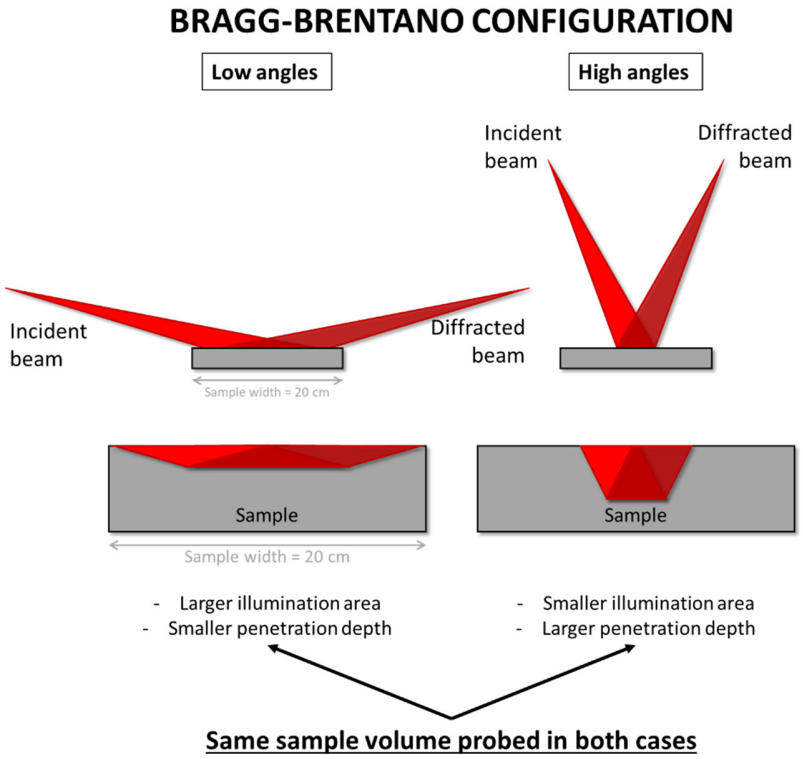

Figure S2. Probed sample volume at different 2θ angles in Bragg Brentano configurations

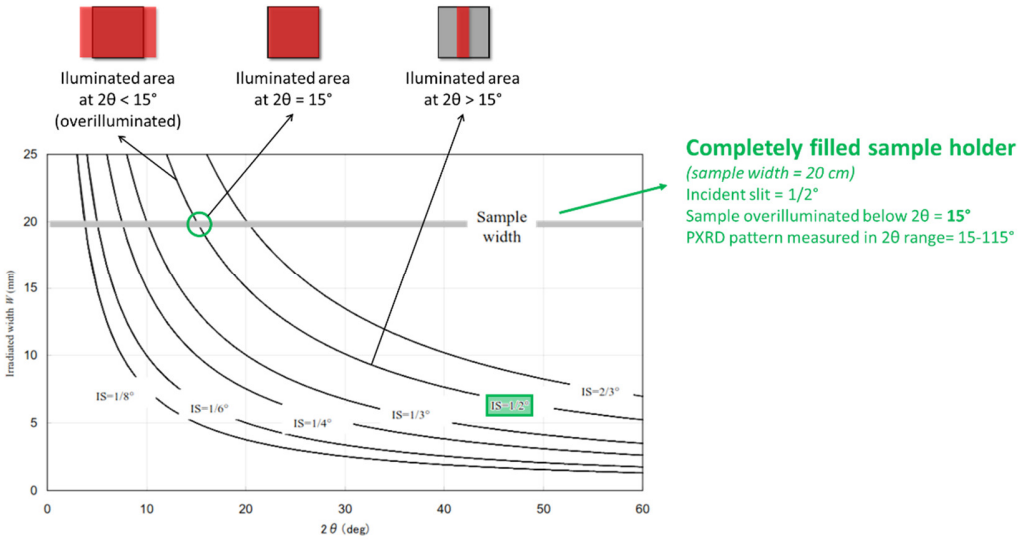

Figure S3. PXRD measurements when the amount of sample is enough to fill the sample holder (sample width = 20 cm). Figure adapted from Rigaku SmartLab user manual.

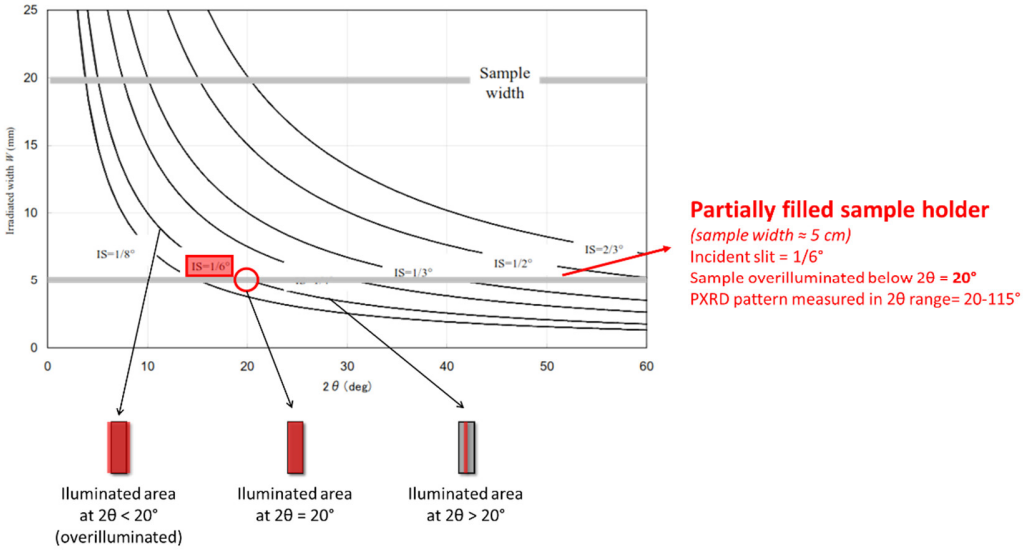

Figure S4. PXRD measurements when the amount of sample only allows for partially filling the sample holder (sample width ≈ 5 cm). Figure adapted from Rigaku SmartLab user manual.

2.2. Rietveld refinements

Crystallographic description of the Rietveld phases

Table S1. Crystallographic description of $CoFe_2O_4$ (spinel). Space group: *Fd*-3*m* (227), total multiplicity: 192.

Atom	Wyckoff position	Atomic position			Site Occupancy in percentage	Calculated Site Occupancy
		x	y	z		
O^{2-}	32e	0.242	0.242	0.242	100%	0.16667
Co^{2+} (Td)	8b	$^3/_8$	$^3/_8$	$^3/_8$	33.3%	0.01389
Fe^{3+} (Td)	8*b*	$^3/_8$	$^3/_8$	$^3/_8$	66.7%	0.02778
Co^{2+} (Oh)	16*c*	0	0	0	33.3%	0.02778
Fe^{3+} (Oh)	16*c*	0	0	0	66.7%	0.05556

Table S2. Crystallographic description of $Co_{0.33}Fe_{0.67}O$ (monoxide). Space group: *Fm*-3*m* (225), total multiplicity: 192.

Atom	Wyckoff position	Atomic position			Site Occupancy in percentage	Calculated Site Occupancy
		x	y	z		
O^{2-}	4b	$^1/_2$	$^1/_2$	$^1/_2$	100%	0.02083
Co^{2+}	4a	0	0	0	33.3%	0.00694
Fe^{2+}	4*a*	0	0	0	66.7%	0.01389

Table S3. Crystallographic description of CoFe (alloy). Space group: *Pm*-3*m* (221), total multiplicity: 48.

Atom	Wyckoff position	Atomic position			Site Occupancy in percentage	Calculated Site Occupancy
		x	y	z		
Co^0 (site 1)	1a	0	0	0	100%	0.02083
Fe^0 (site 2)	1*b*	$^1/_2$	$^1/_2$	$^1/_2$	100%	0. 02083

Table S4. Crystallographic description of Co_2Fe (alloy). Space group: *Pm*-3*m* (221), total multiplicity: 48.

Atom	Wyckoff position	Atomic position			Site Occupancy in percentage	Calculated Site Occupancy
		x	y	z		
Co^0 (site 1)	1a	0	0	0	100%	0.02083
Co^0 (site2)	1b	$^1/_2$	$^1/_2$	$^1/_2$	33.3%	0. 00694
Fe^0 (site 2)	1*b*	$^1/_2$	$^1/_2$	$^1/_2$	66.7%	0.01389

Table S5. Crystallographic description of Co_2Fe_3 (alloy). Space group: *Pm*-3*m* (221), total multiplicity: 48.

Atom	Wyckoff position	Atomic position			Site Occupancy in percentage	Calculated Site Occupancy
		x	y	z		
Fe^0 (site 1)	1a	0	0	0	100%	0.02083
Fe^0 (site2)	1b	$1/2$	$1/2$	$1/2$	20%	0.00417
Co^0 (site 2)	1*b*	$1/2$	$1/2$	$1/2$	80%	0.01666

Graphical representation

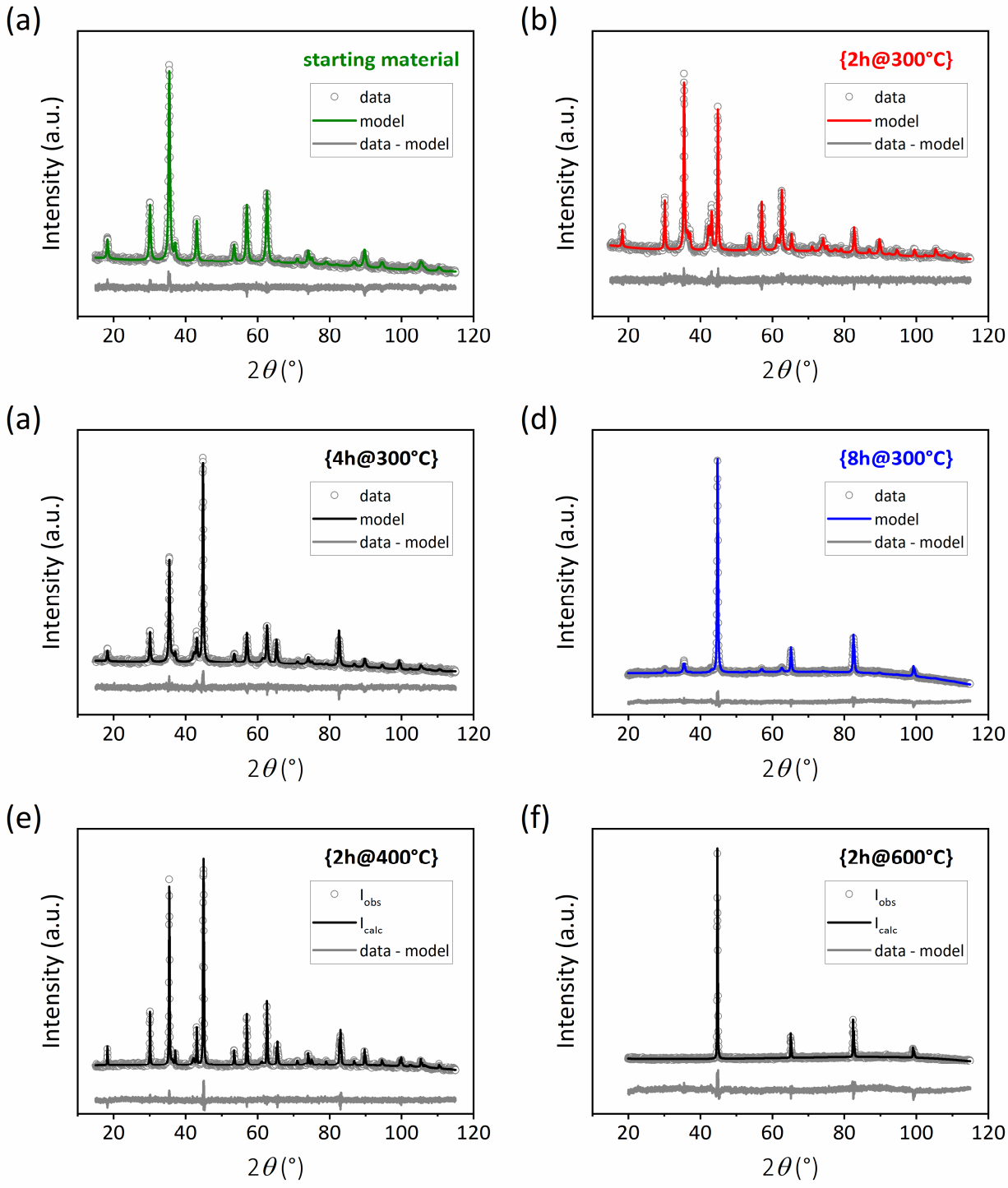

Figure S5. PXRD data and Rietveld models for all samples.

2.3. Influence of additional parameters on the composition and crystallite size

Pressure of reducing gas

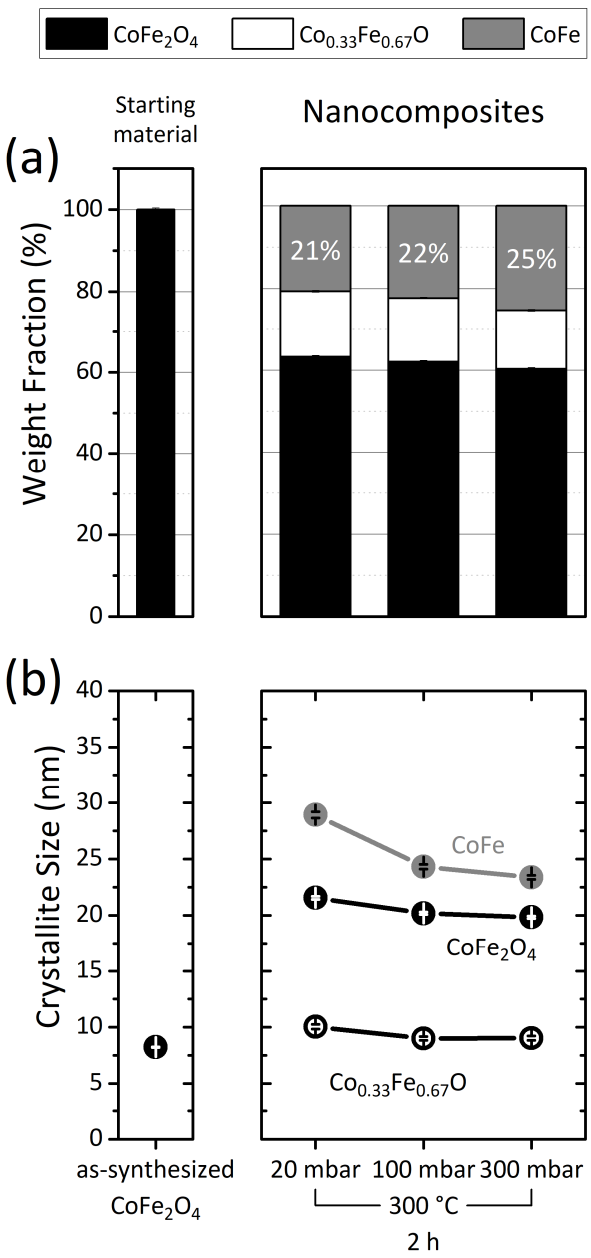

Figure S6. (a) Weight fractions and (b) volume-averaged crystallite sizes extracted from Rietveld analysis of PXRD data collected for 2-hour-long reduction experiments conducted at 300 °C and variable gas pressures. The starting $CoFe_2O_4$ material had an average size of 14.4(1) nm.

Crystallite size of the starting $CoFe_2O_4$ material

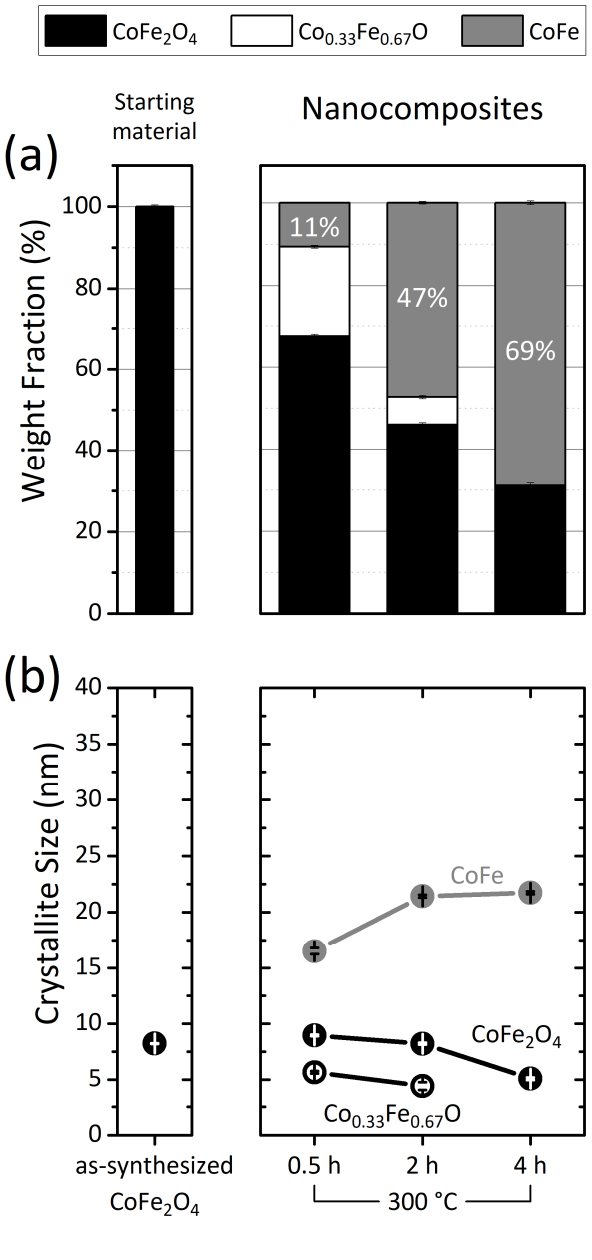

Figure S7. (a) Weight fractions and (b) volume-averaged crystallite sizes extracted from Rietveld analysis of PXRD data collected for reduction experiments conducted at 300 °C, 20 mbar, and a variable duration on a starting $CoFe_2O_4$ material with an average size of 8.2(1) nm.

3. Magnetic hysteresis

3.1. Room temperature magnetic hysteresis (300 K)

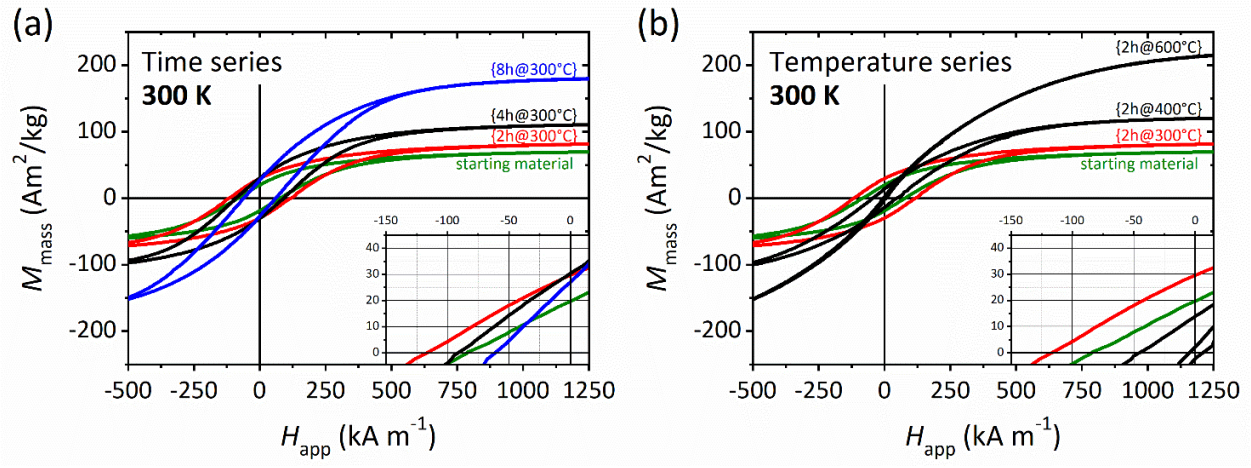

Figure S8. Mass magnetization *versus* applied field at 300 K for (a) the time series of experiments and (b) the temperature series . The insets in each graph is a magnification of the second quadrant of the corresponding hysteresis loop.

3.2. Low temperature magnetic hysteresis (10 K)

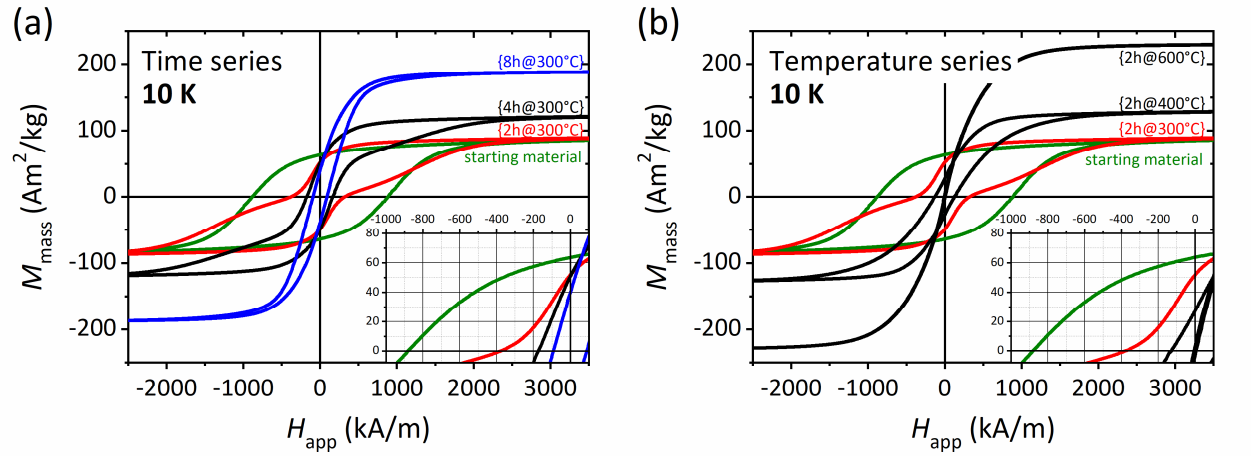

Figure S9. Mass magnetization *versus* applied field at 10 K for (a) the time series of experiments and (b) the temperature series . The insets in each graph is a magnification of the second quadrant of the corresponding hysteresis loop.

Table S6. Saturation magnetization, M_s, remanence, M_r, and coercivity, H_c, extracted from magnetic hysteresis measured at 10 K. The errors on the values are calculated from the uncertainties on the linear fits.

Sample	10 K			
	M_s	M_r	H_c	
	(Am^2/kg)	(Am^2/kg)	(kA/m)	(kOe)
Starting material	90.3(2)	63.73(3)	880(20)	11.0(2)
{2h@300°C}	92.4(7)	51.79(9)	379(3)	4.77(4)
{4h@300°C}	125(1)	50.8(2)	172(2)	2.16(3)
{8h@300°C}	190(1)	39.8(2)	92(2)	1.15(2)
{2h@400°C}	131(1)	27.5(1)	129(2)	1.62(2)
{2h@600°C}	231(1)	2.6(2)	4.57(4)	0.0574(5)

3.3. Coupling and decoupling at low temperature (LT) and room temperature (RT): Further interpretation of the shape of the loops

A 2-step reversal at LT does not always imply that the nanocomposite is decoupled at RT. Actually, decoupling at LT for composites effectively coupled at RT has been observed before for different systems.[1,2] This is a consequence of the increase in magnetic anisotropy that hard phases generally undergo at LT. For instance, the H_c of the starting $CoFe_2O_4$ powders is about 10 times larger at LT than it is at RT. As a consequence of the enhanced anisotropy at LT, the domain wall thickness of the hard phase becomes smaller. According to the theory, soft and hard phases can only be effectively coupled as long as the dimension of the soft phase does not exceed double the size of the hard phase domain thickness.[3,4] Therefore, the anisotropy increase occurring when lowering the measurement temperature may result in the condition for effective exchange-coupling no longer being met. Liu *et al.* concluded that cooperative (single-step) reversal of two interacting (exchange-coupled) grains or particles occurs when $K_1 \leq A_{ex}/< D >^2$, where K_1 is the first anisotropy constant of the hard grain, while the second grain is considered ideally soft, A_{ex} is the exchange stiffness and <*D*> is the diameter of the interacting particles or grains.[2]

However, we do not think this is the reason behind LT decoupling in the nanocomposites described here. For instance, a 2-step reversal at LT is observed for {4h@300°C}, which contains 38.9(2)% metallic alloy with an average crystallite diameter of 26.0(2) nm. If the values of K_1 and A_{ex} in this particular system were favoring a "Liu decoupling" at LT, then the effect should be much more pronounced for {2h@400°C}, which has approx. the same amount of metal (wt.% = 37.8(8)%) but much larger crystallites (mixture of 46.3(8) and 61(2) nm). Instead, a more single-phase-like loop is collected for {2h@400°C} at LT. Therefore, in our samples, the presence of two switching fields at LT can be safely attributed to a weak exchange-coupling between the hard and the soft phases, while a single-step reversal is assigned to a nano-composite with a high degree of exchange-coupling.

References

1 D. Goll, M. Seeger and H. Kronmüller, Magnetic and microstructural properties of nanocrystalline exchange coupled PrFeB permanent magnets, *J. Magn. Magn. Mater.*, 1998, **185**, 49–60.

2 J. P. Liu, R. Skomski, Y. Liu and D. J. Sellmyer, Temperature dependence of magnetic hysteresis of RCo_x:Co nanocomposites (R=Pr and Sm), *J. Appl. Phys.*, 2000, **87**, 6740–6742.

3 T. Schrefl, H. Kronmüller and J. Fidler, Exchange hardening in nano-structured two-phase permanent magnets, *J. Magn. Magn. Mater.*, 1993, **127**, L273–L277.

4 R. Skomski and J. Coey, Giant energy product in nanostructured two-phase magnets, *Phys. Rev. B*, 1993, **48**, 15812–15816.